Three-dimensional flat band evolution between pyrochlore and perovskite lattices with enhanced anomalous Hall effect

Minjun Wang, Wei Jiang,[*] and Yugui Yao

Centre for Quantum Physics, Key Laboratory of Advanced Optoelectronic Quantum Architecture and Measurement (MOE), and Beijing Key Laboratory of Nanophotonics and Ultrafine Optoelectronic Systems, School of Physics, Beijing Institute of Technology, Beijing 100081, China

Distinct from the flat band in two dimensions, the three-dimensional (3D) flat band and the corresponding physics have been relatively unexplored. Here, based on tight-binding models, we present a theoretical study of the evolution of the 3D flat band between pyrochlore and perovskite lattices, which are structurally interconvertible through diagonal strain and host double-degenerate flat bands. We discovered the presence of a persistent 3D flat band during the transition, which is stabilized by a robust compact localized state within the preserved kagome plane perpendicular to the diagonal direction. Furthermore, under the influence of spin-orbit coupling and Zeeman field, we can consistently achieve a magnetic Weyl semimetal state during this transition process due to the unique 3D flat band nature. Pairs of Weyl points form near the conserved flat band, leading to a large anomalous Hall conductivity (AHC) peak right at the energy of the flat band. Interestingly, we also observe an enhanced AHC during the transition from pyrochlore to perovskite lattice due to the enlarged momentum separation between Weyl points and the superimposition with another AHC peak from the dispersive Dirac bands.

I. INTRODUCTION

A system with a flat band that has a momentum-independent energy and infinite effective mass is known to be an ideal platform for exploring the strong correlation effects among electrons [1–9], which has garnered widespread attention. Various exotic quantum phenomena have been theoretically proposed, such as room-temperature ferromagnetism [10–12], Mott physics [5,13], unconventional superconductivity [14,15], Wigner crystallization [6,16], and nontrivial topological properties [17–20], a few of which have been experimentally confirmed [21–23]. Partially benefited from the high tunability and rich varieties of candidate materials, most of those studies have focused on the two-dimensional (2D) systems [24–26], especially in the recently extensively studied twisted bilayer systems [27–31] and/or crystals with kagome lattice [32–35]. Lately, several experimental studies have shown evidence of the existence of a three-dimensional (3D) flat band in the pyrochlore lattice [36,37], i.e., 3D kagome, which has opened a novel avenue in exploring exotic quantum physics related to the flat band. Although theoretical research on 3D flat bands has existed for a long time for both single-particle [38–40] and electron-electron correlated scenarios [41,42], the exploration of the distinctive features of 3D flat bands is still relatively rare compared to their 2D counterpart.

Before the experimental demonstration of the 3D flat band, there were several theoretical studies that explored the formation of 3D flat bands in various lattices and proposed their unique topological and transport properties [20,40,43–48]. Among those limited few lattices that host the 3D flat band, the two well-known pyrochlore and perovskite (i.e., 3D Lieb) lattices, which can be viewed as a 3D version of the 2D kagome and Lieb lattices, show many intriguing similarities, such as the uncommon double-degenerate flat bands and their coexistence with the Dirac band [39,45]. Those unique resemblances can be traced back to their structural equivalence, i.e., one corner-site and three edge-center states in the unit cell. Similar to their 2D counterpart [49,50], pyrochlore and perovskite lattices are also interconvertible by applying strain along the diagonal direction. It would be interesting to study the evolution of the flat band and the corresponding topological states during the transition, which may provide some insight in revealing their peculiar properties in 3D systems.

In this study, we delve into the intriguing structure transition between the pyrochlore and the perovskite structures by systematically investigating the evolution of the 3D flat band through analysis of their unique compacted localized states (CLSs) [51–53] and exploring their topological properties using the tight-binding model Hamiltonian. Our investigation reveals that despite the variation in lattice symmetry during this transition, at least one flat band remains consistently present throughout the entire process. Furthermore, we meticulously examine the alterations in CLS corresponding to the persisting flat band as it evolves during the structure transition. Moreover, we investigate the topological properties considering both the spin-orbit coupling (SOC) [40] and Zeeman field effect, which yields a robust magnetic Weyl semimetal phase during the transition, as confirmed from the Fermi arc and topological invariant calculations. More interestingly, we found a surprising enhancement of the anomalous Hall
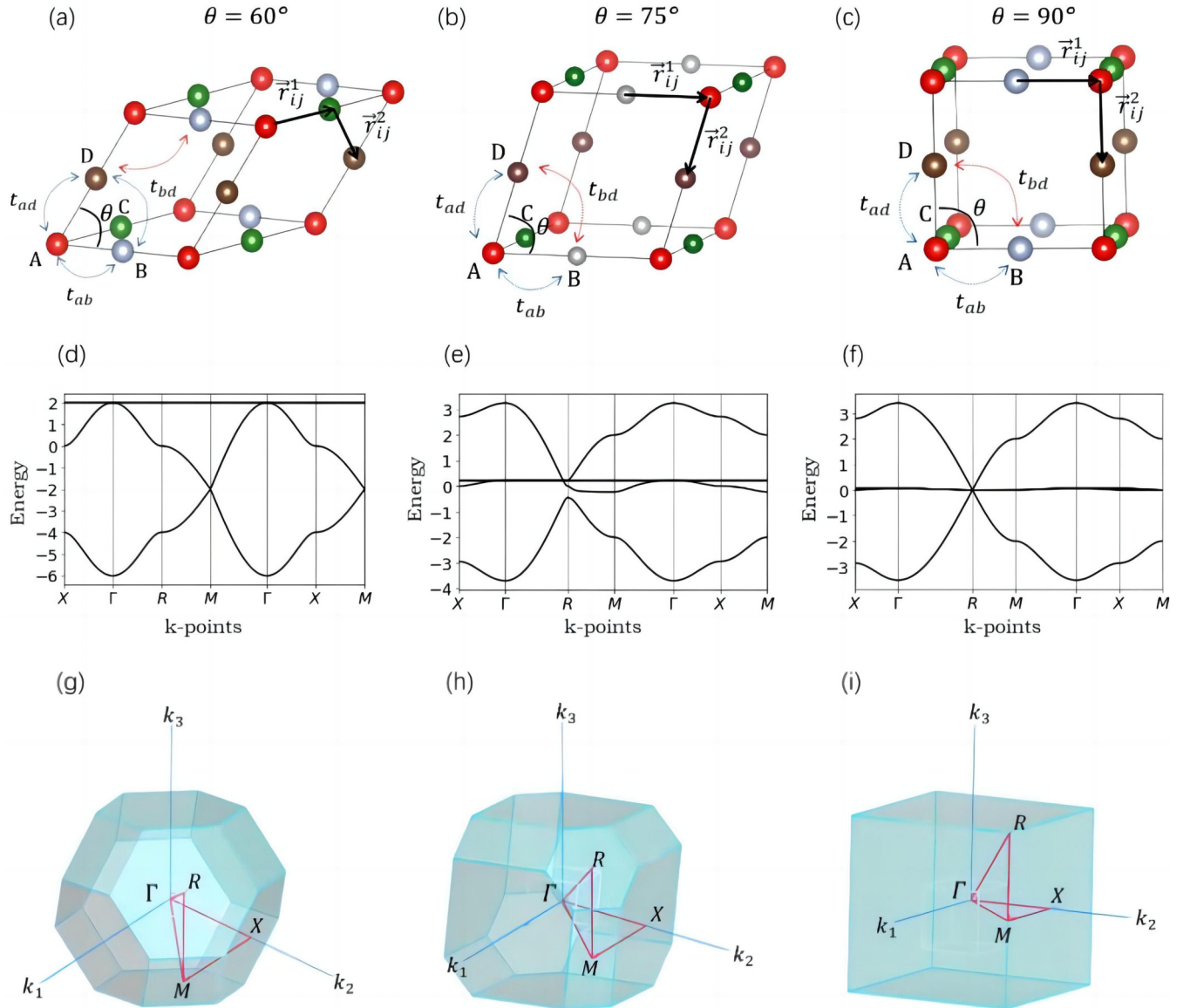
*wjiang@bit.edu.cn

FIG. 1. (a)–(c) The lattice crystal structure of a pyrochlore lattice, transition lattice, and perovskite lattice, and (d)–(f) the corresponding band structure along high-system k paths for the three lattices with the NN hopping $t = -1$. (g)–(i) The first Brillouin zone and high-symmetry k-point paths of the pyrochlore lattice, transition lattice, and perovskite lattice.

conductivity during the lattice transformation process, which can be attributed to the enlarged Weyl point separation and superposition of different Weyl points due to the unique 3D flat band.

II. TRANSITION BETWEEN PYROCHLORE AND PEROVSKITE LATTICES

The structural similarity between pyrochlore and perovskite lattices can be clearly seen in Fig. 1, which contains one corner site A and three edge-center sites B, C, and D in the unit cell. The transformation can be easily achieved by applying a compressive or tensile strain along the diagonal direction, with the angle θ between edges changing from $60°$ (pyrochlore) to $90°$ (perovskite) during the transition, as shown in Fig. 1(b). To investigate the electronic

evolution between pyrochlore and perovskite lattices, we begin by considering the single-orbital tight-binding model on the pyrochlore lattice.

Pyrochlore lattice. The spinless Hamiltonian for this system can be expressed as follows:

$$\mathcal{H} = \sum_i \epsilon_i c_i^\dagger c_i + \sum_{\langle i,j \rangle} t_{ij} c_i^\dagger c_j + \sum_{\langle\langle i,j \rangle\rangle} t'_{ij} c_i^\dagger c_j + \text{H.c.,} \quad (1)$$

where $c_i^\dagger$ and c_j represent the creation and annihilation operators, respectively, ϵ_i denotes the on-site energy, which is set to be zero, and t_{ij} and t'_{ij} denote the hopping amplitudes between the nearest-neighbor (NN) and next-nearest-neighbor (NNN) sites, as highlighted in Fig. 1 by blue and red arrows, respectively. Similar to the approach applied in the previous study about the transition between the kagome and Lieb lattice

[49], the NNN hopping term t'_{ij} is empirically set to decay exponentially with the increasing distance and is defined as

$$t'_{ij} = t e^{\frac{n(a_0 - a_{ij})}{a_0}}, \qquad (2)$$

in which parameters a_0 and a_{ij} denote the distances between the NN and NNN sites, respectively. It is important to note that the NNN hopping term could significantly influence the flatness of the flat band [20,54]. In order to preclude the influence of NNNs when the lattice becomes a pyrochlore/perovskite structure and retain their influence during the lattice transformation process, an appropriate empirical value of $n = 10$ is chosen.

The band structure of Eq. (1) can be obtained by transforming $\mathcal{H}$ into momentum space as $\mathcal{H} = \sum_k \Psi_k^\dagger H_k \Psi_k$ with $\Psi_k^\dagger = (c_{Ak}^\dagger, c_{Bk}^\dagger, c_{Ck}^\dagger, c_{Dk}^\dagger)$. The matrix Hamiltonian with only NN hopping on the pyrochlore lattice is therefore obtained as

$$H_{\mathbf{k}} = t \begin{pmatrix} 0 & 1 + e^{-i\mathbf{k}\mathbf{a}_1} & 1 + e^{-i\mathbf{k}\mathbf{a}_2} & 1 + e^{-i\mathbf{k}\mathbf{a}_3} \\ & 0 & 1 + e^{-i\mathbf{k}(\mathbf{a}_2 - \mathbf{a}_1)} & 1 + e^{-i\mathbf{k}(\mathbf{a}_3 - \mathbf{a}_1)} \\ & & 0 & 1 + e^{-i\mathbf{k}(\mathbf{a}_3 - \mathbf{a}_2)} \\ & & & 0 \end{pmatrix}, \qquad (3)$$

where t is the NN hopping parameter, and $\mathbf{a}_1 = (1, 0, 0)$, $\mathbf{a}_2 = (1/2, \sqrt{3}/2, 0)$, $\mathbf{a}_3 = (1/2, \sqrt{3}/6, \sqrt{6}/3)$ are the three basic unit vectors. Due to the fact that the NNN hopping is much smaller than the NN hopping, the NNN hopping is ignored. Solving the Hamiltonian yields a pair of energetically degenerate flat bands with $E = -2t$ on the top or bottom of the Dirac bands depending on the sign of t, which can be clearly seen in the plotted band structure for the case with $t = -1$, as shown in Fig. 1(d). Here, we will only focus on the flat band related phenomena rather than the Dirac band. The eigenfunctions for the two flat bands are

$$\psi_{\mathbf{k}}^1 = c_1 \begin{pmatrix} e^{-i\mathbf{k}(\mathbf{a}_2 - \mathbf{a}_1)} - 1 \\ e^{i\mathbf{k}\mathbf{a}_1} - e^{-i\mathbf{k}(\mathbf{a}_2 - \mathbf{a}_1)} \\ 1 - e^{i\mathbf{k}\mathbf{a}_1} \\ 0 \end{pmatrix} \qquad (4)$$

and

$$\psi_{\mathbf{k}}^2 = c_2 \begin{pmatrix} e^{-i\mathbf{k}(\mathbf{a}_3 - \mathbf{a}_1)} - 1 \\ e^{i\mathbf{k}\mathbf{a}_1} - e^{-i\mathbf{k}(\mathbf{a}_3 - \mathbf{a}_1)} \\ 0 \\ 1 - e^{i\mathbf{k}\mathbf{a}_1} \end{pmatrix}, \qquad (5)$$

where $c_1 = [6 - 2\cos(\mathbf{k}\mathbf{a}_1 - \mathbf{k}\mathbf{a}_2) - 2\cos\mathbf{k}\mathbf{a}_1 - 2\cos\mathbf{k}\mathbf{a}_2]^{-1/2}$ and $c_2 = [6 - 2\cos(\mathbf{k}\mathbf{a}_1 - \mathbf{k}\mathbf{a}_3) - 2\cos\mathbf{k}\mathbf{a}_1 - 2\cos\mathbf{k}\mathbf{a}_3]^{-1/2}$.

To better understand the strict localization of those flat band states, a compact localized state (CLS) with finite amplitude only within a restricted region in real space can usually be constructed, as a manifestation of the destructive interference. Therefore, based on the aforementioned eigenfunctions, we calculated the relevant CLS (unnormalized) through an inverse Fourier transformation [55]. Due to the double degeneracy of the flat bands, there are two sets of CLSs ($A_{0,R}^{(1)}$ and $A_{0,R}^{(2)}$), which have the forms shown below in Eqs. (6) and (7)
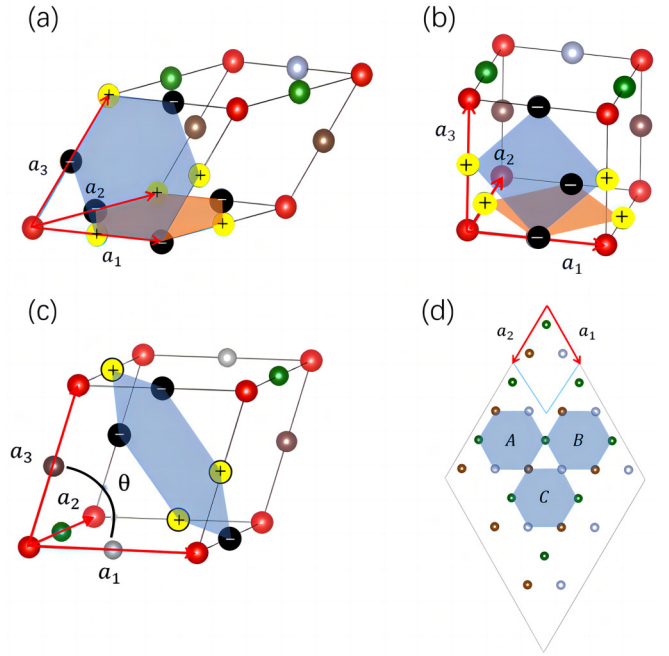

FIG. 2. Schematic of three types of CLSs of a (a) pyrochlore lattice, (b) perovskite lattice, and (c) transition lattice. The CLSs are exhibited by blue and orange shaded areas. The yellow and black dots represent positive and negative phases, respectively. (d) The CLS for the transition lattice with $\theta = 75°$ in the $(1, 1, 1)$ plane perpendicular to the diagonal direction with A, B, and C represent the translated CLSs, respectively. The quadrilateral formed by the blue dashed line is the in-plane primitive cell.

and illustrated in Fig. 2(a) using blue and orange, respectively. The two CLSs have a similar form as that in the 2D kagome lattice, i.e., hexagonal ring with alternating positive (yellow colored state) and negative (black colored state) phases,

$$A_{0,R}^{(1)} = \begin{pmatrix} \delta_{R, -\mathbf{a}_1 + \mathbf{a}_2} - \delta_{R, 0} \\ \delta_{R, -\mathbf{a}_1} - \delta_{R, -\mathbf{a}_1 + \mathbf{a}_2} \\ \delta_{R, 0} - \delta_{R, -\mathbf{a}_1} \\ 0 \end{pmatrix}, \qquad (6)$$

$$A_{0,R}^{(2)} = \begin{pmatrix} \delta_{R, -\mathbf{a}_1 + \mathbf{a}_3} - \delta_{R, 0} \\ \delta_{R, -\mathbf{a}_1} - \delta_{R, -\mathbf{a}_1 + \mathbf{a}_3} \\ 0 \\ \delta_{R, 0} - \delta_{R, -\mathbf{a}_1} \end{pmatrix}. \qquad (7)$$

Perovskite lattice. By applying compressive strain to the pyrochlore lattice along the diagonal direction, we can achieve the perovskite structure with $\theta = 90°$, as shown in Fig. 1(c). The matrix Hamiltonian that describes the perovskite lattice can be expressed as (the effect of NNN hopping t'_{ij} can be ignored)

$$H_{\mathbf{k}} = t \begin{pmatrix} 0 & 1 + e^{-i\mathbf{k}\mathbf{a}_1} & 1 + e^{-i\mathbf{k}\mathbf{a}_2} & 1 + e^{-i\mathbf{k}\mathbf{a}_3} \\ 1 + e^{i\mathbf{k}\mathbf{a}_1} & 0 & 0 & 0 \\ 1 + e^{i\mathbf{k}\mathbf{a}_2} & 0 & 0 & 0 \\ 1 + e^{i\mathbf{k}\mathbf{a}_3} & 0 & 0 & 0 \end{pmatrix}, \qquad (8)$$

where $\mathbf{a}_1 = (1, 0, 0)$, $\mathbf{a}_2 = (0, 1, 0)$, and $\mathbf{a}_3 = (0, 0, 1)$ are the three basic unit vectors. Interestingly, the band structure also hosts two energetically degenerate flat bands. Different from the pyrochlore lattice that has the flat band on top of the Dirac bands, the flat band in the perovskite lattice is located in the middle of the Dirac band at $E = 0$, as can be seen in Fig. 1(f). Further, we can obtain the corresponding eigenvectors,

$$
\psi_{\mathbf{k}}^1 = c_1 \begin{pmatrix} 0 \\ -e^{ik_x} - e^{i(k_x - k_y)} \\ 1 + e^{ik_x} \\ 0 \end{pmatrix}, \tag{9}
$$

$$
\psi_{\mathbf{k}}^2 = c_2 \begin{pmatrix} 0 \\ -e^{ik_x} - e^{i(k_x - k_z)} \\ 0 \\ 1 + e^{ik_x} \end{pmatrix}, \tag{10}
$$

where $c_1 = [4 + 2\cos k_x + 2\cos k_y]^{-1/2}$ and $c_2 = [4 + 2\cos k_x + 2\cos k_z]^{-1/2}$. As illustrated in Fig. 2(b), one can clearly see the geometry of the two CLSs,

$$
A_{0,R}^{(3)} = \begin{pmatrix} 0 \\ -\delta_{R,-\mathbf{a}_1} - \delta_{R,-\mathbf{a}_1+\mathbf{a}_2} \\ \delta_{R,0} + \delta_{R,-\mathbf{a}_1} \\ 0 \end{pmatrix}, \tag{11}
$$

$$
A_{0,R}^{(4)} = \begin{pmatrix} 0 \\ -\delta_{R,-\mathbf{a}_1} - \delta_{R,-\mathbf{a}_1+\mathbf{a}_3} \\ 0 \\ +\delta_{R,0} + \delta_{R,-\mathbf{a}_1} \end{pmatrix}, \tag{12}
$$

that correspond to the ψ_k^1 and ψ_k^2. Each 3D CLS has a similar form to the 2D Lieb lattice with four edge-center states with

alternating phases [55], as highlighted by the black and yellow colors with plus and minus sign, respectively.

However, as a result, the CLS obtained by linearly superposing the eigenstates in momentum space will miss the eigenstate at $\mathbf{k} = (0, 0, 0)$, and the CLSs in the pyrochlore lattice are therefore incomplete [39,55], i.e., there are eigenstates that cannot be described by the simple lattice translation of those CLSs due to the existence of singular touching points between the flat and dispersive bands [39]. Examining the band structure of the pyrochlore lattice, it becomes evident that the two degenerate flat bands and the dispersion band indeed intersect at the Γ point.

Three additional noncontractable loop states are needed to form the subspace of the flat band for a complete description [39]. On the other hand, for the perovskite lattice, the flat band touches both the upper and lower dispersive bands at the R point, where one of the touching points can be eliminated by altering the on-site energy of the lattice while preserving the flat band. Therefore, one of the touching points is not immovable [39,55] and has no impact on the incompleteness of the CLSs. There are also three additional states that need to be complemented besides the CLSs to fully describe the flat band for the perovskite lattice similar to the pyrochlore case.

Transition lattice. Because of both the structural and electronic similarity between the pyrochlore and perovskite lattices, it would be interesting to study the intermediate lattice during the structural transition. Therefore, we create a Hamiltonian that varies with θ to describe the transition lattice. It is important to note that the NNN hopping term is defined as $t'_{ij} = t e^{\frac{n(a_0 - a_{ij})}{a_0}}$, which can be rewritten as $t'_{ij} = t f(\theta)$, with $f(\theta) = \exp\{n[1 - (2 - 2\cos\theta)^{1/2}]\}$. The $f(\theta)$ varies as a function of NNN distance a_{ij} that changes with the parameter θ, as illustrated in Fig. 1(b). With this information, we can construct the Hamiltonian for the transition state as follows:

$$
H_{\mathbf{k}} = t \begin{pmatrix} 0 & 1 + e^{-i\mathbf{k}\mathbf{a}_1} & 1 + e^{-i\mathbf{k}\mathbf{a}_2} & 1 + e^{-i\mathbf{k}\mathbf{a}_3} \\ & 0 & f(\theta)(1 + e^{-i\mathbf{k}(\mathbf{a}_2-\mathbf{a}_1)}) & f(\theta)(1 + e^{-i\mathbf{k}(\mathbf{a}_3-\mathbf{a}_1)}) \\ & & 0 & f(\theta)(1 + e^{-i\mathbf{k}(\mathbf{a}_3-\mathbf{a}_2)}) \\ & & & 0 \end{pmatrix}, \tag{13}
$$

where $\mathbf{a}_1 = (1, 0, 0)$, $\mathbf{a}_2 = (\cos\theta, \sin\theta, 0)$, and $\mathbf{a}_3 = [\cos\theta, y, (1 - \cos^2\theta - y^2)^{1/2}]$ are the three θ-dependent basic unit vectors with $y = \cot\theta(1 - \cos\theta)$. Interestingly, distinct from the evolution in the 2D systems between the kagome and Lieb lattice that completely destroys the flat band [49], there is one flat band that remains robust against the structural transformation in the 3D systems with the eigenvalue of $E = -2t f(\theta)$, as shown in Fig. 1(e).

During the transition from pyrochlore to perovskite lattice, one of the two double-degenerate flat bands on top of the dispersive bands becomes dispersive, while the other one remains flat and gradually moves to the middle that forms the double-degenerate flat bands in the middle of Dirac bands [Figs. 1(d)–1(f)]. To understand the underlying physics, we calculate the related eigenstate that corresponds to the robust flat band for the transition lattice, which can be described as

follows:

$$
\psi_{\mathbf{k}} = c \begin{pmatrix} 0 \\ e^{-i\mathbf{k}\mathbf{a}_2} - e^{-i\mathbf{k}\mathbf{a}_3} \\ e^{-i\mathbf{k}\mathbf{a}_3} - e^{-i\mathbf{k}\mathbf{a}_1} \\ e^{-i\mathbf{k}\mathbf{a}_1} - e^{-i\mathbf{k}\mathbf{a}_2} \end{pmatrix}, \tag{14}
$$

with $c = [6 - 2\cos\mathbf{k}(\mathbf{a}_3 - \mathbf{a}_2) - 2\cos\mathbf{k}(\mathbf{a}_1 - \mathbf{a}_3) - 2\cos\mathbf{k}(\mathbf{a}_1 - \mathbf{a}_2)]^{-1/2}$, and the corresponding CLS expressed as

$$
A_{0,R} = \begin{pmatrix} 0 \\ \delta_{R,\mathbf{a}_2} - \delta_{R,\mathbf{a}_3} \\ \delta_{R,\mathbf{a}_3} - \delta_{R,\mathbf{a}_1} \\ \delta_{R,\mathbf{a}_1} - \delta_{R,\mathbf{a}_2} \end{pmatrix}. \tag{15}
$$

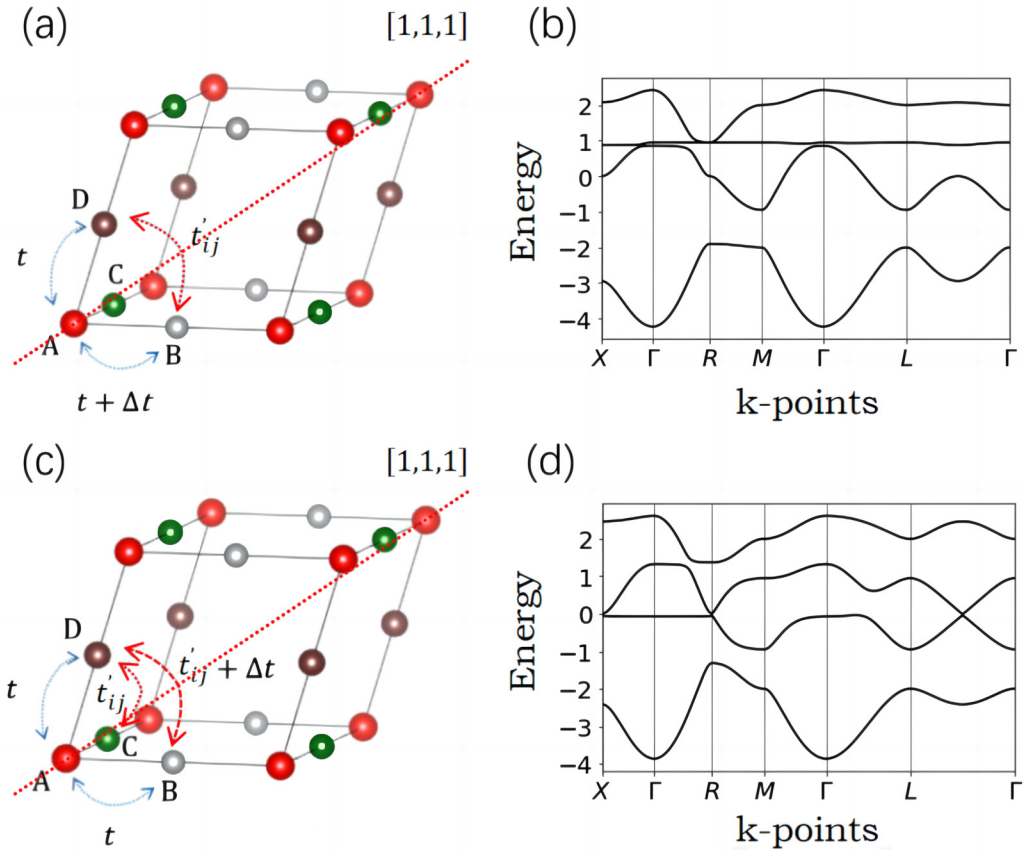The CLS for the transition state is visually depicted in Fig. 2(c), which shares a similar geometry feature as that of

FIG. 3. (a) The structure of transition lattice $\theta = 65°$, but one of the NN hopping strengths (blue arrows) changes to $t + \Delta t$. (b) The band structure of the transition lattice with $t = -1$ and $\Delta t = 0.5$. (c), (d) same as (a) and (b), but with different NNN hopping (red arrows).

the kagome lattice. When further examining the plane where the CLS is situated, i.e., perpendicular to the diagonal direction, it becomes apparent that the plane's structure is identical to that of a 2D kagome lattice, as can be clearly seen in Fig. 2(d). As the lattice structure undergoes changes between pyrochlore and perovskite, this plane continuously persists, regardless of the value of θ. The only variation lies in the alteration of the lattice constants, but the CLS remains intact, as shown in the blue shaded areas in Fig. 2(d). We note that there are different CLS selections for the flat bands besides the current CLSs shown in Fig. 2. We can also choose the hexagon within the (1,1,1) kagome plane as one of the two CLSs, which can better demonstrate the continuous transformation between the pyrochlore and perovskite lattices (more details are given in Appendix A).

To better understand the robust CLS that is located within the kagome plane perpendicular to the diagonal direction, we analyzed the geometric symmetry of the transition structure. Along the diagonal direction, the Hamiltonian's C_3 symmetry significantly impacts the formation of flat bands. To further verify the relationship between symmetry and the flat band, we purposely varied the hopping parameters to break the C_3 rotational symmetry. This can be done by either modifying the NN or NNN interaction. If one of the NN hopping strengths, t_{ij}, is modified, as illustrated in Fig. 3(a), the Hamiltonian no longer possesses C_3 rotational symmetry, leading to the destruction of the flat band, as shown in Fig. 3(b). Similarly, the change of one of the NNN hopping parameters, t'_{ij}, also

leads to the breakdown of the flat band in the 3D Brillouin zone, as shown in Figs. 3(c) and 3(d).

III. TOPOLOGICAL PROPERTIES

It has been shown that the double-degenerate flat band in 3D systems can lead to certain unique topological properties beyond their 2D counterpart [20,49], such as the 3D topological insulator [20] and enhanced anomalous Hall effect in magnetic Weyl semimetals [20,56]. It would be interesting to also explore the topological evolution during the transition between pyrochlore and perovskite lattices. In this section, we will explore the topological properties of the lattices in transition by further considering an intrinsic NNN spin-orbit coupling (SOC) interaction as described in Eq. (16) and Zeeman-type exchange splitting term to the Hamiltonian, as described in Eq. (17) [46],

$$H_{SOC} = i\lambda \sum_{\langle\langle ij\rangle\rangle\alpha\beta} \left(\vec{r}^1_{ij} \times \vec{r}^2_{ij}\right) \cdot \sigma_{\alpha\beta} c^\dagger_{i\alpha} c_{j\beta}, \quad (16)$$

$$H_z = \lambda_z \sum_{i\alpha} c^\dagger_{i\alpha} \sigma_{z\alpha\alpha} c_{j\alpha}, \quad (17)$$

where $c^\dagger_{i\alpha}$ and $c_{j\beta}$ represent the creation and annihilation operators, respectively, and α and β denote different spins. $\sigma = (\sigma_x, \sigma_y,$ and $\sigma_z)$ are the Pauli matrices. $\vec{r}^1_{ij}$ and $\vec{r}^2_{ij}$ are the two NN bonds that electrons traverse from site j to i, as shown in Figs. 1(a)–1(c), which are used to describe the SOC. λ and λ_z indicate the strength of the SOC and Zeeman field, respectively.
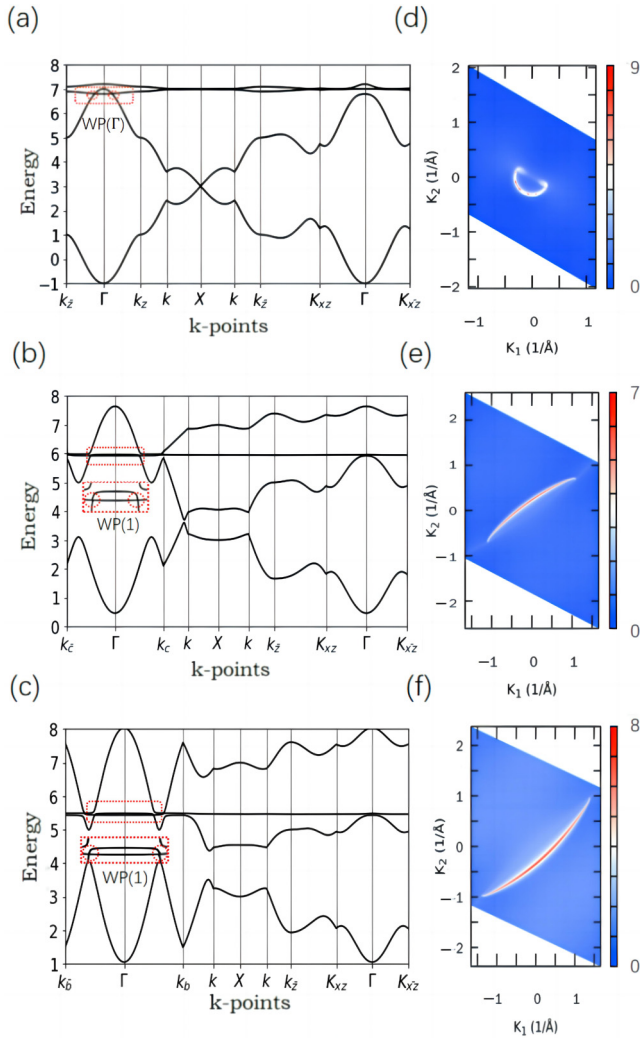
FIG. 4. The energy band structure (choose upper branch, lower branch is symmetric to the upper) with SOC ($\lambda = -0.2t$) and Zeeman term $\lambda_z = 5t$ of the (a) pyrochlore lattice, (b) transition lattice $\theta = 65°$, and (c) transition lattice $\theta = 70°$ along the high-symmetry k path in the Brillouin zone. Insets: The Weyl points with red dashed boxes. (d)–(f) The corresponding Fermi arc state in the (1,1,1), (0.0.1), (0,0,1) plane, respectively.

Magnetic Weyl semimetal. For simplicity, in this work, we will investigate the systems in the large Zeeman field limit with $\lambda_z = 5t$ to focus on the interaction between one set of spins related to the flat band. When considering the large Zeeman splitting, the position of the spin-up and spin-down flat bands corresponds to an electron filling of 3/8 and 7/8, respectively. When we further consider the SOC effect, the system becomes a time-reversal symmetry-breaking magnetic Weyl semimetal. Pairs of Weyl points (WPs) are generated near the quasiflat band, which aligns with what has been previously reported [20,46], as illustrated in Fig. 4(a). We note that there are multiple pairs of Weyl nodes near the quasiflat band, while only one single pair of Weyl nodes, WP(Γ), is formed by the quasiflat band and the dispersive band near the Γ point, as highlighted by the red square in Fig. 4(a). We further conducted calculations of two transition lattices with $\theta = 65°$ and $\theta = 70°$, respectively. The band structures are

shown in Figs. 4(b) and 4(c), which shows that as the lattice angle undergoes variations, the two quasiflat bands gradually separate into one quasiflat band and one dispersive band. Interestingly, near the Γ point, the quasiflat band remains intersecting with the dispersive band, leading to the formation of a robust Weyl semimetal phase with a single pair of Weyl nodes, as highlighted by the inset in Figs. 4(b) and 4(c).

Additionally, we have conducted calculations for the Fermi arc state (i.e., surface state of a topological semimetal that is terminated onto the projections of the Weyl nodes on the surface) of the pyrochlore lattice and two transition lattices near WP(1) using the WANNIERTOOLS package [57,58]. For this analysis, we have selected the surface where the pair of Weyl points formed by the quasiflat band is located. Figures 4(d)–4(f) display the Fermi arc state of the three systems with different θ, which confirm the formation of magnetic Weyl semimetal phases. We notice that these Weyl points will also gradually move away from the Γ points while transforming from pyrochlore to the perovskite lattices, resulting in a widening Fermi arc. It has been reported that the Weyl points' separation in the momentum space plays a crucial role in determining the strength of the anomalous Hall effect [20,56]. Therefore, we further calculate the anomalous Hall conductivity of those systems.

Anomalous Hall effect. The anomalous Hall conductivity is calculated based on the Kubo formula with

$$\sigma_{xy} = -\frac{e^2}{\hbar} \int_{BZ} \frac{d^3k}{(2\pi)^3} \sum_n f_{n\mathbf{k}} \Omega_n^{xy}(\mathbf{k}) \tag{18}$$

and

$$\Omega_n^{xy}(\mathbf{k}) = -\sum_{n' \neq n} \frac{2\,\text{Im}[\langle u_{n\mathbf{k}}|v_{x\mathbf{k}}|u_{n'\mathbf{k}}\rangle \langle u_{n'\mathbf{k}}|v_{y\mathbf{k}}|u_{n\mathbf{k}}\rangle]}{(\epsilon_{n'\mathbf{k}} - \epsilon_{n\mathbf{k}})^2}, \tag{19}$$

which integrates the Berry curvature Ω_n^{xy} of all the occupied states throughout the whole Brillouin zone. For the pyrochlore structure, we find that near the two energetically degenerate quasiflat bands, there is a wide peak (P1) constructed of two nearly degenerate peaks, labeled P1(a) and P1(b), respectively, as shown in Fig. 5(a). Such anomalous Hall conductivity (AHC) peak can be attributed to the formation of multiple Weyl points due to the two quasiflat bands, which contribute large Berry curvatures [20]. In addition, there is an even larger AHC peak near the crossing point ("Dirac point") formed by the two Dirac bands due to the gap opening driven by the SOC and Zeeman field.

We further calculate the AHC for the transition states and the perovskite lattice. As the lattice structure changes, the peak P1(a) gradually diminishes and eventually disappears, leaving only P1(b), denoted as P1 hereafter. At this point, the anomalous Hall conductivity always exhibits two robust peaks, i.e., P1 and P2, during the structural transformation. Interestingly, P1 and P2 are shifting along with the movement of the flat band and the "Dirac point," respectively, as illustrated in Figs. 5(b) and 5(c). We note that the sign of the P1 also flips during the transition, which may be caused by a change of Weyl pairs chirality as the Berry curvature is directly related to the chirality of the Weyl point [20]. To better demonstrate this point, we directly calculated the chirality of the Weyl pairs formed near the Γ point by the
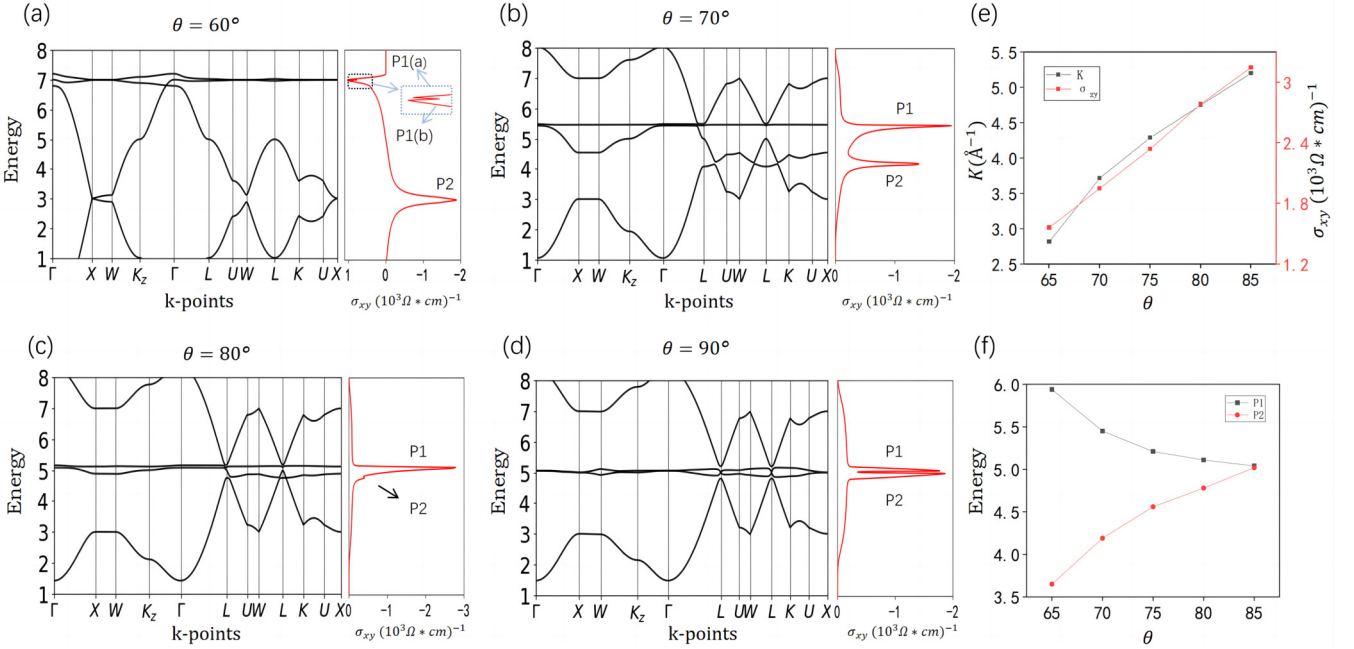
FIG. 5. (a)–(d) The band structure along the high-symmetry k path and AHC of the pyrochlore lattice, transition lattice $\theta = 70°$, $\theta = 80°$, and perovskite lattice. (e) Evolution of K for WP(1) and their corresponding AHC, with different θ. (f) Evolution of energy of P1 and P2.

flat band and the lower dispersion band at lattice angles of 60 and 60.5 degrees, respectively. As shown in Appendix B, with the slight change in lattice angle, the Weyl pairs change from the kz direction to near the (111) direction, which leads to a chirality change and therefore a sign change of the AHC peak near the flat band. However, by continuing to change the lattice angle (60.5–90 degrees), the Weyl pair distribution remains in a similar direction and the chirality of the Weyl points remains unchanged, so the sign of the AHC will no longer change. Most importantly, we see a clear enhancement of P1 with the increase of θ, which agrees very well with the increased momentum separation between the Weyl points formed by the quasiflat bands, as demonstrated in Fig. 4.

To further verify this point, we extracted the momentum separation between the pair of Weyl points formed by the quasiflat band and the dispersive band, and also the magnitude of the AHC P1 as a function of the θ. We note that due to the double-degenerate quasiflat bands in the pyrochlore lattice and perovskite lattice, they give rise to numerous Weyl points in the same energy. However, in the transition states, only one band remains flat that forms one pair of Weyl points near the Γ point, as shown in Fig. 4. To better capture the relationship between the separation among one pair of Weyl points [WP(1)] and the AHC, we plot only the results from the transition states. The results are summarized in Fig. 5(e), which shows a very good linear relationship between the two, consistent with the theories proposed before, i.e., $\sigma_{xy} = (e^2 K/4\pi^2)$ (K is the momentum separation between the pair of Weyl points) [20,56]. Furthermore, with variations in the lattice structure, the two AHC peaks gradually approach each other and merge in the middle of the energy spectrum, leading to even larger AHC when $\theta \approx 85°$. This becomes evident from the plot of the energy evolution of the two peaks as a function of θ, as shown in Fig. 5(f). When the lattice structure transforms into the perovskite lattice, two degenerate quasiflat bands reappear

between the two dispersive bands. At this point, two split peaks emerge again near the quasiflat bands i.e., P1 and P2, leading to a reduction in the maximum AHC peak, as illustrated in Fig. 5(d).

IV. CONCLUSION AND PERSPECTIVE

In summary, we systematically studied the flat band evolution during the lattice transformation between pyrochlore and perovskite lattices and explored their compacted localized states, topological features, and transport behaviors. One of the flat bands is found to be robust during the lattice evolution process with the corresponding CLS located in an invariant 2D kagome lattice plane, as protected by the C3 rotational symmetry along the diagonal axis. The inclusion of both SOC and Zeeman field drives the system into magnetic Weyl semimetal states, which remain robust and shows an intriguing AHC enhancement while transferred from a pyrochlore to perovskite lattice. Such an AHC enhancement can be attributed to the enlarged Weyl pair separation as well as the superimposition of multiple AHC peaks driven by the evolution of 3D flat bands during structural transformation.

It is important to note that this work only studied the single-particle scenario of the 3D flat band based on the tight-binding method. The further consideration of Coulomb interaction between electrons could potentially lead to more exotic quantum phenomena, which, however, is beyond the scope of this work. We note that the study of the 3D flat band is still in its infancy, where their unique exotic quantum phenomena await further exploration and the realization in real materials will play a more critical role for the breakthrough. Several pyrochlore materials with flat bands have been studied with large anomalous Hall effect and/or ferromagnetism [2,20,46,59]; however, realistic materials to realize the lattice transformation through sufficient stress are yet to be explored.
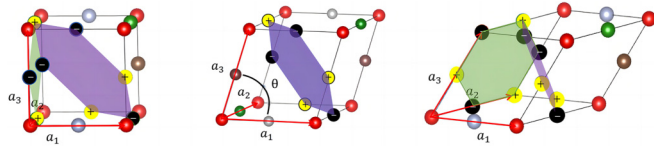
FIG. 6. Schematic of three types of CLSs of a pyrochlore lattice, perovskite lattice, and transition lattice, respectively. The CLSs are represented by purple and green polygons, with yellow and black spheres denoting the different phases.

APPENDIX A: CONTINUOUS CLSs

We note that there are actually four different CLSs for the two degenerate flat bands in the pyrochlore and perovskite lattices, in which only two are independent and selected for the demonstration. Beside the CLSs presented in Fig. 2, we can also choose the hexagon within the (1,1,1) kagome plane as one of the two CLSs, as shown below in Fig. 6. The CLSs are represented by purple and green polygons, which clearly shows the continuous transformation during the lattice transition, i.e., the wave function corresponding to the CLS shown by purple hexagons is continuously changing, while the green CLS only exists in the perfect pyrochlore/perovskite lattice and disappears when there is a small change in the lattice. This is reasonable as only one of the two flat bands remains flat during the transition, while the other one exists only for the perfect pyrochlore/perovskite lattice.

APPENDIX B: CHIRALITY OF WEYL POINTS

In this Appendix, we demonstrate that the chirality of the Weyl points near the Γ point will change when there is a slight change in the lattice structure. We calculated the chirality of
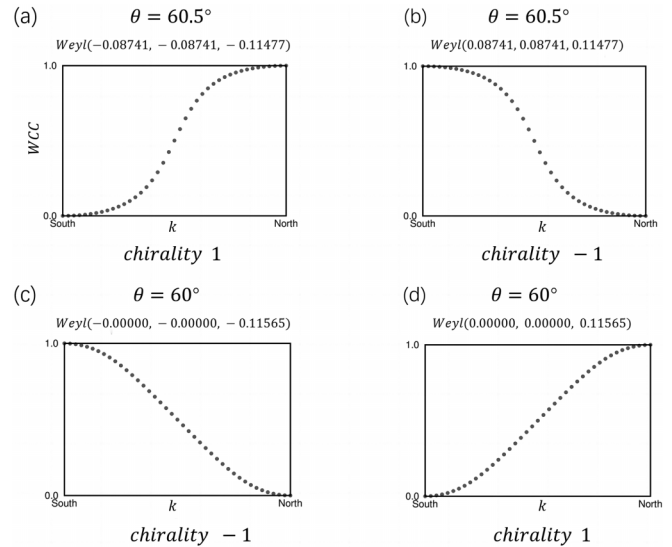

FIG. 7. The chirality change of the Weyl points formed near the flat band. (a), (b) The momentum position $[(-0.0874, -0.0874, -0.1147), (0.0874, 0.0874, 0.1147)]$ and chirality of a pair of Weyl points near the Γ point as derived from the change of Wannier charge center for a transition lattice with 60.5 degrees. (c), (d) The momentum position $[(0, 0, 0.11565), (0, 0, -0.11565)]$ and chirality of a pair of Weyl points near the Γ point for a pyrochlore lattice with 60 degrees. The Weyl pair changes from the k_z direction to near the (111) direction during the transition from 60 to 60.5 degrees, which leads to a chirality change.

the Weyl points at lattice angles of 60 degrees and 60.5 degrees, respectively [representing the handedness of the Weyl points by calculating the change in Wannier charge center (WCC)], as shown in Fig 7. With the slight change in lattice angle, the Weyl pairs also slightly change in the momentum space. More importantly, the Weyl pair changes from the k_z direction to near the (111) direction, which leads to a chirality change and therefore a sign change of the AHC peak near the flat band. However, by continuing to change the lattice angle (60.5–90 degrees), the Weyl pair distribution remains in a similar direction and the chirality of the Weyl points remain unchanged, so the sign of the AHC will no longer change.

[1] H. Wang, J.-H. Gao, and F.-C. Zhang, Phys. Rev. B **87**, 155116 (2013).

[2] I. Hase, T. Yanagisawa, Y. Aiura, and K. Kawashima, Phys. Rev. Lett. **120**, 196401 (2018).

[3] W. Häusler, Phys. Rev. B **91**, 041102(R) (2015).

[4] O. Derzhko, J. Richter, and M. Maksymenko, Intl. J. Mod. Phys. B **29**, 1530007 (2015).

[5] H. C. Po, L. Zou, A. Vishwanath, and T. Senthil, Phys. Rev. X **8**, 031089 (2018).

[6] C. Wu, D. Bergman, L. Balents, and S. Das Sarma, Phys. Rev. Lett. **99**, 070401 (2007).

[7] A. Julku, S. Peotta, T. I. Vanhala, D.-H. Kim, and P. Törmä, Phys. Rev. Lett. **117**, 045303 (2016).

[8] W. Jiang, Z. Liu, J.-W. Mei, B. Cui, and F. Liu, Nanoscale **11**, 955 (2019).

[9] W. Jiang, X. Ni, and F. Liu, Acc. Chem. Res. **54**, 416 (2021).

[10] A. Mielke, J. Phys. A: Math. Gen. **24**, L73 (1991).

[11] A. Mielke, J. Phys. A: Math. Gen. **24**, 3311 (1991).

[12] W. Jiang, H. Huang, and F. Liu, Nat. Commun. **10**, 2207 (2019).

[13] S. Gao, S. Zhang, C. Wang, W. Tao, J. Liu, T. Wang, S. Yuan, G. Qu, M. Pan, S. Peng, Y. Hu, H. Li, Y. Huang, H. Zhou, S. Meng, L. Yang, Z. Wang, Y. Yao, Z. Chen, and T. Qian, Phys. Rev. X **13**, 041049 (2023).

[14] S. Miyahara, S. Kusuta, and N. Furukawa, Physica C: Superconduct. **460-462**, 1145 (2007).

[15] G. E. Volovik, J. Supercond. Novel Magn. **26**, 2887 (2013).

[16] C. Wu and S. Das Sarma, Phys. Rev. B **77**, 235107 (2008).

[17] E. Tang, J.-W. Mei, and X.-G. Wen, Phys. Rev. Lett. **106**, 236802 (2011).

[18] K. Sun, Z. Gu, H. Katsura, and S. Das Sarma, Phys. Rev. Lett. **106**, 236803 (2011).

[19] T. Neupert, L. Santos, C. Chamon, and C. Mudry, Phys. Rev. Lett. **106**, 236804 (2011).

[20] W. Jiang, D. J. P. de Sousa, J.-P. Wang, and T. Low, Phys. Rev. Lett. **126**, 106601 (2021).

[21] M. Hyrkäs, V. Apaja, and M. Manninen, Phys. Rev. A **87**, 023614 (2013).

[22] F. Baboux, L. Ge, T. Jacqmin, M. Biondi, E. Galopin, A. Lemaître, L. Le Gratiet, I. Sagnes, S. Schmidt, H. E. Türeci, A. Amo, and J. Bloch, Phys. Rev. Lett. **116**, 066402 (2016).

[23] H. Ozawa, S. Taie, T. Ichinose, and Y. Takahashi, Phys. Rev. Lett. **118**, 175301 (2017).

[24] H. Liu, S. Meng, and F. Liu, Phys. Rev. Mater. **5**, 084203 (2021).

[25] N. Regnault, Y. Xu, M.-R. Li, D.-S. Ma, M. Jovanovic, A. Yazdani, S. S. P. Parkin, C. Felser, L. M. Schoop, N. P. Ong, R. J. Cava, L. Elcoro, Z.-D. Song, and B. A. Bernevig, Nature (London) **603**, 824 (2022).

[26] A. Bhattacharya, I. Timokhin, R. Chatterjee, Q. Yang, and A. Mishchenko, npj Comput. Mater. **9**, 101 (2023).

[27] R. Bistritzer and A. H. MacDonald, Proc. Natl. Acad. Sci. USA **108**, 12233 (2011).

[28] Y. Cao, V. Fatemi, S. Fang, K. Watanabe, T. Taniguchi, E. Kaxiras, and P. Jarillo-Herrero, Nature (London) **556**, 43 (2018).

[29] G. Tarnopolsky, A. J. Kruchkov, and A. Vishwanath, Phys. Rev. Lett. **122**, 106405 (2019).

[30] Z. Zhang, Y. Wang, K. Watanabe, T. Taniguchi, K. Ueno, E. Tutuc, and B. J. LeRoy, Nat. Phys. **16**, 1093 (2020).

[31] S. Lisi, X. Lu, T. Benschop, T. A. de Jong, P. Stepanov, J. R. Duran, F. Margot, I. Cucchi, E. Cappelli, A. Hunter, A. Tamai, V. Kandyba, A. Giampietri, A. Barinov, J. Jobst, V. Stalman, M. Leeuwenhoek, K. Watanabe, T. Taniguchi, L. Rademaker *et al.*, Nat. Phys. **17**, 189 (2021).

[32] D. Kim and F. Liu, Phys. Rev. B **107**, 205130 (2023).

[33] M. Kang, S. Fang, L. Ye, H. C. Po, J. Denlinger, C. Jozwiak, A. Bostwick, E. Rotenberg, E. Kaxiras, J. G. Checkelsky, and R. Comin, Nat. Commun. **11**, 4004 (2020).

[34] H. Zhao, H. Li, B. R. Ortiz, S. M. L. Teicher, T. Park, M. Ye, Z. Wang, L. Balents, S. D. Wilson, and I. Zeljkovic, Nature (London) **599**, 216 (2021).

[35] S. Okamoto, N. Mohanta, E. Dagotto, and D. N. Sheng, Commun. Phys. **5**, 198 (2022).

[36] J. P. Wakefield, M. Kang, P. M. Neves, D. Oh, S. Fang, R. McTigue, S. Y. Frank Zhao, T. N. Lamichhane, A. Chen, S. Lee, S. Park, J.-H. Park, C. Jozwiak, A. Bostwick, E. Rotenberg, A. Rajapitamahuni, E. Vescovo, J. L. McChesney, D. Graf, J. C. Palmstrom *et al.*, Nature (London) **623**, 301 (2023).

[37] J. Huang, C. Setty, L. Deng, J.-Y. You, H. Liu, S. Shao, J. S. Oh, Y. Guo, Y. Zhang, Z. Yue, J.-X. Yin, M. Hashimoto, D. Lu, S. Gorovikov, P. Dai, M. Z. Hasan, Y.-P. Feng, R. J. Birgeneau, Y. Shi, C.-W. Chu *et al.*, arXiv:2304.09066.

[38] S. Nishino and M. Goda, J. Phys. Soc. Jpn. **74**, 393 (2005).

[39] D. L. Bergman, C. Wu, and L. Balents, Phys. Rev. B **78**, 125104 (2008).

[40] H.-M. Guo and M. Franz, Phys. Rev. Lett. **103**, 206805 (2009).

[41] Z. Gulácsi and D. Vollhardt, Phys. Rev. Lett. **91**, 186401 (2003).

[42] Z. Gulácsi and D. Vollhardt, Phys. Rev. B **72**, 075130 (2005).

[43] M. Trescher and E. J. Bergholtz, Phys. Rev. B **86**, 241111(R) (2012).

[44] A. Lau, T. Hyart, C. Autieri, A. Chen, and D. I. Pikulin, Phys. Rev. X **11**, 031017 (2021).

[45] C. Weeks and M. Franz, Phys. Rev. B **85**, 041104(R) (2012).

[46] Y. Zhou, K.-H. Jin, H. Huang, Z. Wang, and F. Liu, Phys. Rev. B **99**, 201105(R) (2019).

[47] G. Liu, P. Zhang, Z. Wang, and S.-S. Li, Phys. Rev. B **79**, 035323 (2009).

[48] Z. Wang and P. Zhang, New J. Phys. **12**, 043055 (2010).

[49] W. Jiang, M. Kang, H. Huang, H. Xu, T. Low, and F. Liu, Phys. Rev. B **99**, 125131 (2019).

[50] L.-K. Lim, J.-N. Fuchs, F. Piéchon, and G. Montambaux, Phys. Rev. B **101**, 045131 (2020).

[51] B. Sutherland, Phys. Rev. B **34**, 5208 (1986).

[52] H. Aoki, M. Ando, and H. Matsumura, Phys. Rev. B **54**, R17296 (1996).

[53] W. Maimaiti, A. Andreanov, H. C. Park, O. Gendelman, and S. Flach, Phys. Rev. B **95**, 115135 (2017).

[54] W.-F. Tsai, C. Fang, H. Yao, and J. Hu, New J. Phys. **17**, 055016 (2015).

[55] J.-W. Rhim and B.-J. Yang, Phys. Rev. B **99**, 045107 (2019).

[56] A. A. Burkov, Phys. Rev. Lett. **113**, 187202 (2014).

[57] Q. Wu, S. Zhang, H.-F. Song, M. Troyer, and A. A. Soluyanov, Comput. Phys. Commun. **224**, 405 (2018).

[58] M. P. L. Sancho, J. M. L. Sancho, J. M. L. Sancho, and J. Rubio, J. Phys. F **15**, 851 (1985).

[59] J. G. Azadani, W. Jiang, J.-P. Wang, and T. Low, Phys. Rev. B **102**, 155144 (2020).